Simulation of airborne nanoparticles transport, deposition and aggregation: Experimental validation of a CFD-QMOM approach

Romain Guichard, Emmanuel Belut

Simulation of airborne nanoparticles transport, deposition and aggregation: experimental validation of a CFD-QMOM approach

Romain Guichard*, Emmanuel Belut

Institut National de Recherche et de Sécurité, Vandœuvre-lès-Nancy, F-54500, France.

* Corresponding author: romain.guichard@inrs.fr

Highlights

- 3D simulation of the dynamics of non-spherical nanoparticles is evaluated.
- Computed and experimentally measured airflow and aerosol properties are compared.
- Two aerosols with different composition, morphology and size are considered.
- CFD-QMOM convincingly predicts the aggregation of airborne nanoparticles.

Graphical abstract

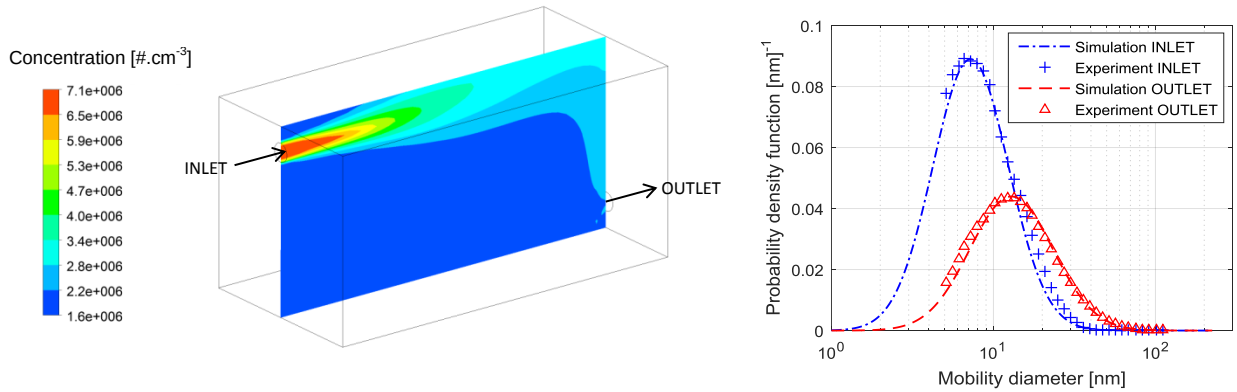

Abstract

This paper evaluates the ability of a CFD-QMOM modeling approach to predict the dynamics of the particle size distribution (PSD) of airborne non-spherical nanoparticles. The experimental case of a small chamber ventilated by a steady turbulent airflow at moderate Reynolds number is considered. In this configuration, the aerosol dynamics is essentially driven by convection and turbulent-Brownian aggregation. Numerical results are compared to available experimental data: space-resolved PSD measurements for the particulate phase and mean airflow velocity, turbulence kinetic energy and mean age of air profiles for the gas phase. Given the experimental uncertainties, a good agreement between

experimental and simulation results is found. The use of two types of aerosols, with identical initial concentration but different compositions, sizes and morphologies highlights the influence of these parameters on aggregation kinetics. The highest particle number reduction due to aggregation is achieved for the smallest and least compact nanoparticles.

Keywords

Computational fluid dynamics; Quadrature method of moments; Indoor nanoparticles; Aggregation; Deposition; Transport.

1. Introduction

The increasing use of nanotechnologies and manufactured nanomaterials leads inevitably to a higher likelihood of release of airborne nanoparticles in the environment or at the workplace. Considering the existing worries or proven hazards (Hoet et al., 2004; Oberdörster et al., 2005; Wichmann and Peters, 2000) regarding inhalation of such aerosols, there is a need of developing models able to predict their transport, deposition and physico-chemical changes. Suitable quantitative models may help evaluating workers and public exposure, preventing this exposure by designing suitable mitigation strategies, or assisting the nanotoxicologists in designing experimental setups for inhalation studies.

In manufacturing plants, airborne ultrafine particles at high concentrations can be encountered, where their size distribution (PSD) can quickly change from their source to the environment through aggregation (Fuchs, 1964). Since the aerodynamic diameter of particles will determine their deposition likelihood in the upper and lower airways, an important aspect of a proper human exposure model is hence its ability to predict the evolution of the PSD in space and time.

In that context, models based on Computational Fluid Dynamics (CFD) may provide a detailed estimate of exposure to airborne nanoparticles indoors, provided that they account for this aggregation process. In CFD models, two points of view are generally discussed when examining the modeling of particles aggregation, namely Eulerian and Lagrangian (Berlemont et al., 2001; Claudotte et al., 2010; Fox et al., 2008; Laurent et al., 2004; Mohaupt et al., 2011; Sommerfeld, 2001). The Eulerian viewpoint is preferred when computationally effective treatments of particle collision and aggregation are necessary. Eulerian aggregation models are based on the well-known population balance equation (Friedlander, 2000; Lambin and Gaspard, 1982; Mulholland and Baum, 1980). Since solving this equation with a direct numerical method is time-consuming, three main approximate approaches are available: the discrete method initiated by Smoluchowski (1917), the sectional method (Kostoglou, 2007; Kumar et al., 2006; Kumar and Ramkrishna, 1996), and the method of moments originally

derived by Hulburt and Katz (1964). Sectional methods were developed to avoid numerical diffusion errors inherent to the discrete method, but they remain computationally expensive. For this reason, the moments based methods constitute an attractive alternative when the aggregation process needs to be introduced in a CFD model (Cheng et al., 2009; Cheng and Fox, 2010; Marchisio et al., 2003b; Prat and Ducoste, 2006; Wang et al., 2005).

Several closure techniques of the method of moments have been developed such as log-normal MOM (Lee et al., 1984; Pratsinis, 1988), Gamma MOM (Williams, 1985), Gaussian quadrature MOM (QMOM) and its variant PD-QMOM (Marchisio et al., 2003a; McGraw, 1997), direct QMOM (Marchisio and Fox, 2005), fixed QMOM (Alopaeus et al., 2006), pth-order-polynomial MOM (Barrett and Jheeta, 1996), MOM with interpolative closure (MOMIC) (Frenklach, 2002), and Taylor series expansion MOM (TEMOM) (Yu et al., 2008; Yu and Lin, 2009). The methods of Lee et al. (1984), Pratsinis (1988) and Williams (1985) assume a particular shape of the PSD, which is too restrictive for studying a wide range of aerosols, particularly when the input of the model comes from experimental measurements. The method of Barrett and Jheeta (1996) presents similar limitations since it makes assumptions on the set of moments. Other methods of moments like the MOMIC and the TEMOM (Frenklach, 2002; Yu et al., 2008; Yu and Lin, 2009) are very interesting to achieve a low computational cost, especially when particle dynamics have to be combined with computationally demanding mechanisms (combustion, reactive flow, etc.). However, for aerosols undergoing both Brownian and turbulent aggregation, between the free-molecular and the continuous regime, the accuracy of these methods has not been tested. Moreover, to reconstruct the particle size distribution from the moments, there is a need for moment methods that have demonstrated their ability to allow high quadrature orders. The work of John et al. (2007) indeed states that at least three points of quadrature (six moments) are required to correctly represent a PSD with a single peak and six points of quadrature (twelve moments) are required to reconstruct a PSD with two or three peaks.

In this context, we showed (Guichard et al., 2014b) that the DAE-QMOM approach of Gimbun et al. (2009) was particularly well suited to solve the modelling of aerosol undergoing aggregation in turbulent indoor air conditions with a high quadrature order. A complete CFD model, which used this DAE-QMOM approach for the aggregation of the particulate phase was then presented (Guichard et al., 2014a). It accounts for the transport, the Brownian and turbulent aggregation and the deposition of aerosols with particle size ranging from a few nanometers to a few micrometers. This model was assessed in very simple configurations, like ducts, bends and well-mixed chambers, each configuration allowing the validation of an isolated physical phenomenon (deposition, Brownian or turbulent aggregation, transport, etc.). More recent developments were also proposed in (Guichard et al., 2014b) in order to take into account the effect of morphology on aggregation kinetics and to demonstrate the influence of turbulence. Comparisons with reference experimental data showed the ability of the

modelling approach to predict the PSD shift due to aggregation. However, the validation was limited by the available experimental data.

The experimental validation of the coupling of CFD with the method of moments to investigate the dynamics of two-phase flows where the discrete phase undergoes aggregation has already been addressed in the past for specific applications. Marchisio et al. (2003b) have evaluated the implementation of CFD-QMOM for particles suspended in a Taylor-Couette liquid flow where breakage was in competition with aggregation. However, this situation is quite far from the case of airborne nanoparticles in indoor environments, especially since turbulent aggregation does not occur. The same comment applies to the work of Sung et al. (2011), who investigated nucleation and Brownian aggregation in a turbulent diffusion flame. This as well cannot be used as a reference to evaluate the ability of the CFD-QMOM approach to describe the dynamics of aerosols of nanoparticles in ambient air. Moreover, no spatial characterization of the particle size distributions has been conducted in these works. Other available experiments in the field (Kim et al., 2006, 2003; Koivisto et al., 2012; Seipenbusch et al., 2008; Wentzel et al., 2003) all considered perfectly stirred environments. Consequently, the obtained data were better fitted for the validation of 0-Dimensional models than for CFD models, especially considering the intricate choice of a stirred flow for CFD validation. Another unsatisfied experimental need for CFD concerned the characterization of turbulence, which plays a significant role on aggregation kinetics (Zaichik and Solov'ev, 2002). No turbulence measurements were generally reported in these experiments, except in Kim et al. (2006), who provided only an indirect global characterization of turbulence by fitting deposition curves. Finally, the information concerning the morphology of aggregates is generally missing in these experiments, particularly their collision diameter which significantly affects the aggregation rate.

So far, these drawbacks prevented a straightforward experimental validation of CFD models designed for airborne nanoparticles transport and aggregation, until recently an experiment was specially designed (Belut and Christophe, 2016). The purpose of the present paper is hence to evaluate the performance of the nano-aerosols dynamics model described in Guichard et al. (2014a) as compared to this experimental work. This paper considers the case of two different types of aerosols, namely sodium chloride and copper oxide particles, presenting distinct PSDs, which are steadily injected in an aggregation chamber at moderate Reynolds number. After briefly describing the reference experiment and the model, the simulated airflow results are compared with Laser Doppler Anemometry (LDA) measurements. Then computed and measured PSD properties in the chamber are compared for both aerosols.

2. Experimental reference case

We consider the experiment of Belut and Christophe (2016), who investigated the steady state reached by an aerosol of nanoparticles continuously injected into a ventilated chamber of 0.8×0.4×0.4 m, namely a volume of 0.128 m^3. The inlet and the outlet present circular sections with a diameter of 0.04 m. Their centers are respectively located at 0.055 m of the top and 0.055 m of the bottom in the central plane of the chamber, as sketched in figure 1. The coordinate system referred to in the following subsections is also shown in this figure.

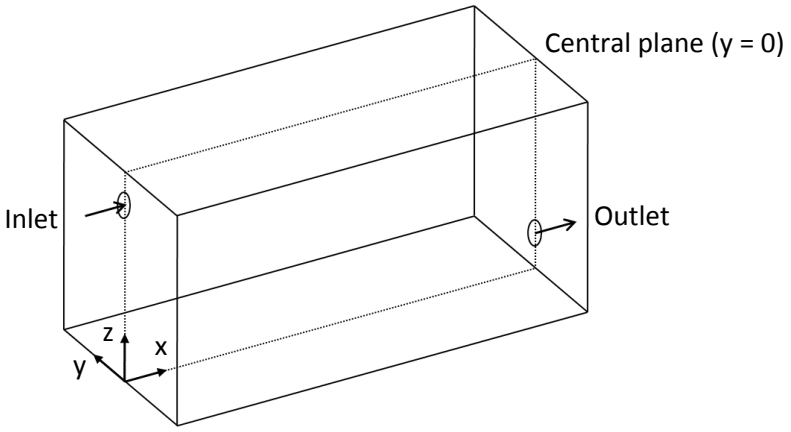

Figure 1 Overview of the ventilated chamber used in Belut and Christophe (2016)

In this experiment, airflow velocity profiles and turbulence parameters were measured by Laser Doppler Anemometry (LDA, Dantec Flow Explorer, Dantec Dynamics, Skovlunde, Denmark). The mean fluid velocity at inlet was 0.589 $m.s^{-1}$ (pipe Reynolds number of 1500, Reynolds number based on the chamber height of 15 000) and the round jet formed by the incoming flow degenerated to turbulence in the chamber. The authors supplemented the characterization of the airflow by providing measurements of the mean age of air at several points in the chamber, which characterizes the air renewal and ventilation homogeneity in the chamber. The transport and aggregation in the chamber of two types of aerosol was considered: the first studied aerosol was composed of polydisperse sodium chloride (*NaCl*) cubes generated by spray-drying, with a geometric mean size of 43.7 nm, a geometric standard deviation of 1.65 and a density of 2170 $kg.m^{-3}$. The second aerosol was composed of polydisperse copper oxide (*CuO*) particles generated by spark discharge, with a geometric mean size of 9.7 nm, a geometric standard deviation of 1.71 and a density of 6315 $kg.m^{-3}$. For both aerosols, measurements of the particle size distribution in terms of electrical mobility diameter were carried out on various vertical profiles throughout the chamber when the steady state was reached. Particle size distributions were sampled thanks to a Scanning Mobility Particle Sizer (SMPS composed of a Grimm 5.403 Condensation Particle Counter linked to a short Differential Mobility Analyser, Vienna type, GRIMM Aerosol Technik GmbH, Ainring, Germany), which allowed measuring the particle size

distribution in terms of mobility diameters in the range [5-350 nm], with a sampling flow rate of 0.3 $l.min^{-1}$. The morphology of aggregates was documented through Transmission Electron Microscopy (TEM) analysis so as to provide additional data concerning the particles monomer size and their effective collision diameter and shape factor.

3. Model

3.1. Airflow modeling

For indoor air applications and for aerosols in general, the Peclet number is very large, *i.e.* aerosol transport is largely dominated by convection. Hence, whichever the method used to model the dispersed phase in the CFD framework, the first step consists in accurately resolving the airflow. For a sufficiently dilute aerosol (volume fraction below 10^{-6}) composed of low-inertia particles (particle relaxation time lower than Kolmogorov's time scale, which in practice is the case for particles with aerodynamic diameters below 10µm for most indoor air applications), it can be assumed that particles do not influence the carrier gas flow (Elghobashi, 1994; Gao and Niu, 2007; Holmberg and Chen, 2003; Holmberg and Li, 1998; Zhao et al., 2004). A one-way coupling approach can hence be used to model the airflow in the present case. For indoor environments, the RANS $k-\varepsilon$ RNG (Yakhot et al., 1992) turbulence model is frequently adopted. In this paper, we then considered this turbulence model, such as implemented in the commercial code Ansys Fluent 15.0 with a finite volume approach. In the present case, the use of a realizable closure model was also enforced by the presence of a round jet. Comparison between predicted airflows and turbulence parameters with the LDA measurements confirm the relevance of this choice for the present application, as highlighted in the result section.

The mesh size was constrained by the deposition formulation for the aerosol described in section 3.3, equation (12), namely the sizes of the first cells near the wall were chosen so that the non-dimensional cell-wall distances were close to $y^+ > 30$. The mesh was composed of 70,000 hexahedral cells with a slight refinement near the inlet and the outlet to improve mesh quality statistics. Another mesh of 500,000 hexahedral cells has also been used to verify the good convergence of the results according to the spatial discretization. Standard wall functions were used for both meshes since most of the wall-adjacent cells were in the logarithmic zone of the turbulent boundary layer profile. At inlet, the velocity and turbulence profiles provided by Belut and Christophe (2016) were imposed as boundary conditions for the simulations. The QUICK discretization scheme was used for momentum equations together with the SIMPLE algorithm for pressure-velocity coupling. The resolution was considered converged when all normalized residuals decreased below 10^{-6}.

3.2. Age of air modeling

The mean age of air τ_a at a given point corresponds to the average time needed by air molecules to reach this point, starting from the air inlet. The mean age of air gives information about the mixing homogeneity in the chamber and is also a good indicator of the residence time of airborne pollution. Since it accounts simultaneously for both mean and turbulent transport, it is a robust way of evaluating the quality of airflow modeling and it can be easily compared to experimental measurements. The mean age of air is modeled by the following advection-diffusion equation in steady-state:

$$U_i \frac{\partial \tau_a}{\partial x_i} = \frac{\partial}{\partial x_i}\left(\left(D_B + D_T \right) \frac{\partial \tau_a}{\partial x_j} \right) + 1, \tag{1}$$

where U_i is the air velocity in the spatial direction i, D_B corresponds to the Brownian diffusivity of air molecules and D_T is the turbulent diffusion coefficient. This transport equation is associated to zero flux boundary conditions at walls and outlet and a Dirichlet boundary condition at inlet with $\tau_a = 0$. It is implemented as a passive scalar transport equation and solved by means of the QUICK discretization scheme.

3.3. Aerosol modeling

Assuming that the airflow is correctly solved and converged, a convenient solution to track the dynamics of an aerosol in indoor environments has been presented by Chen et al. (2006) as a new "Drift-Flux" model. This model has been successfully compared to experiments for two aerosols of 1 µm and 10 µm. In these cases, the aerosol dynamics is governed by transport (both convection and diffusion), gravitational settling and deposition. The "Drift-Flux" model appears very fast and predictive for monodisperse aerosols. However, when a polydisperse aerosol is considered, it becomes necessary to discretize the PSD into sections and then solve one transport equation for each particle size. This sectional method significantly increases the computational cost of the entire simulation, especially when a fine resolution of the PSD is needed. This is the case when considering submicron particles at high concentrations, for which the aggregation phenomenon is significant. Aggregation tends to change the PSD with space and time, which can be accounted for as source terms in the "Drift-Flux" model by solving the population balance equation. As stated in the introduction, such method requires computationally expensive numerical techniques. In order to reduce the computational cost inherent to aggregation, methods of moments have been developed. They consist in tracking only the moments of the particle size distribution, which are defined by:

$$M_k(t) = \int_0^{\infty} n(L,t) L^k dL, \tag{2}$$

where $n(L,t)$ expresses the concentration of particles of size L at time t and $M_k(t)$ is the k^{th} moment of the particle size distribution. However, definition (2) applied to the population balance equation leads to integro-differential equations which cannot be analytically solved in the general case. To overcome this difficulty, we use the DAE-QMOM technique described in Guichard et al. (2014b), which was initially proposed in Gimbun et al. (2009) in a chemical engineering context. It is possible to keep a low computational cost since Marchisio et al. (2003a) showed that the first six moments were sufficient to describe a particle size distribution, *i.e.*, only six transport equations are solved for tracking the dispersed phase flow.

3.3.1. Transport equation

The starting point consists in rewriting the "Drift-Flux" model in terms of moments. Some assumptions can be made when considering low-inertia particles in a ventilated room: the turbulent diffusivity is much larger than the Brownian diffusivity, except in the near wall region where the Brownian diffusivity affects the deposition. Thus the Brownian diffusivity only appears in the deposition flux term and is not considered in the transport equation. Moreover, for particles as small as those considered in present paper (below 200 nm), the settling velocity is lower than 10^{-6} m.s^{-1}, which is two orders of magnitude inferior to Brownian velocity and several orders of magnitude lower than the average flow velocity. Hence, settling is negligible with respect to convective transport by the fluid and to Brownian motion, also observed by Allen (2003). The final transport equation then takes the following form:

$$\frac{\partial M_k(t)}{\partial t} + U_i \frac{\partial M_k(t)}{\partial x_i} = \frac{\partial}{\partial x_i}\left(D_T \frac{\partial M_k(t)}{\partial x_j} \right) + \Pi_{c,k}(t), \tag{3}$$

where U_i is the i^{th} component of the fluid mean velocity and $\Pi_{c,k}(t)$ is the aggregation source term of moment $M_k(t)$. The aggregation source term and the boundary condition used to treat the deposition are detailed in the following subsections. The isotropic turbulent diffusion coefficient D_T is given by:

$$D_T = \frac{\nu_T}{Sc_T}, \tag{4}$$

where Sc_T is the turbulent Schmidt number and ν_T is the fluid turbulent viscosity. The turbulent Schmidt number is usually taken equal to one and the turbulent viscosity is computed as $\nu_T = C_\mu k^2/\varepsilon$, where k and ε respectively represent the turbulence kinetic energy and the turbulence dissipation rate. According to the chosen closure turbulence model, generally realizable or RNG for simulating airflows in ventilated rooms, parameter C_μ takes different values (Shih et al., 1995; Yakhot et al., 1992). The set of equations (3) can be implemented in any CFD solver as passive scalar transport equations including a source term.

3.3.2. Aggregation source term

The temporal change of moments due to the aggregation phenomenon is given by the following population balance equation (Hulburt and Katz, 1964):

$$\Pi_{c,k}(t) = \int_0^\infty \int_0^\infty \beta(L,L') \left(\frac{1}{2} \left(L^3 + L'^3 \right)^{k/3} - L^k \right) n(L) n(L') dL dL', \tag{5}$$

where $\beta(L,L')$ is the aggregation kernel between particles of size L and particles of size L'. The Brownian and turbulent aggregation kernel described in Guichard et al. (2014b) is used. It corresponds to the kernel of Zaichik and Solov'ev (2002) which has been adapted to account for the morphology of aggregates, as:

$$\beta(L,L') = \frac{\sqrt{\beta_B^{col\,2} + \beta_T^{col\,2}}}{1 + \frac{\sqrt{\beta_B^{col\,2} + \beta_T^{col\,2}}}{\beta_B^{agg}} \left(1 - \pi \frac{\chi}{2} + \chi \tan^{-1} \chi \right)}, \tag{6}$$

where β_B^{col} is the Brownian collision kernel for the free-molecular mode, β_B^{coag} is the Brownian aggregation kernel in the continuum mode, β_T^{col} is the turbulent collision kernel and χ is a parameter characterizing the relative contribution of turbulence and Brownian motion on aggregation. The turbulent collision kernel is given by:

$$\beta_T^{col} = \sqrt{\frac{8\pi}{15}} \frac{\sigma^3}{\tau_k}, \tag{7}$$

where τ_K is the Kolmogorov time scale and $\sigma = \left(L_g + L_g'\right)/2$ is the collision radius, depending on geometrical diameters L_g and L_g' which are defined in equation (18). The free-molecular Brownian collision kernel is derived from kinetic theory of gas as:

$$\beta_B^{col} = \sqrt{\frac{8\pi k_B T}{m}}\sigma^2 \ , \tag{8}$$

which includes the Boltzmann constant k_B equal to 1.38×10^{-23} $m^2.kg.s^{-2}.K^{-1}$, the temperature T and the effective mass of particles expressed as $m = m(L)m(L')/\left(m(L)+m(L')\right)$. The mass of a particle with a volume equivalent diameter L is provided by $m(L) = \rho_p \pi L^3/6$, where ρ_p is the particle elemental density. The continuum Brownian aggregation kernel is defined by:

$$\beta_B^{agg} = 2\pi\sigma\left(D_B(L) + D_B(L')\right) \ , \tag{9}$$

where $D_B(L)$ is the Brownian diffusion coefficient. The Brownian diffusion coefficient of a particle of size L is computed by:

$$D_B(L) = \frac{k_B T Cu(L)}{3\pi\mu_f L} . \tag{10}$$

where μ_f is the fluid dynamic viscosity and $Cu(L)$ expresses the Cunningham coefficient that is related to the Knudsen number $Kn(L)$ as:

$$Cu(L) = 1 + Kn(L)\left(1.165 + 0.483\exp\left(-\frac{0.997}{Kn(L)}\right)\right). \tag{11}$$

The Knudsen number is given by $Kn(L) = 2\lambda/L$ where λ is the mean free path of the carrier gas, typically equal to 66 nm for the ambient air at 20 °C.

3.3.3. Boundary condition for the deposition

The particle deposition is taken into account by directly providing the theoretical flux of moments towards the wall. Following the "Dynamic Boundary Layer" model of Nerisson et al. (2011), the concentration profile in the boundary layer is integrated, leading to the following expression of the deposition flux:

$$\Phi_{s,k}(t) = \int_0^{\infty} V_d(L)\, n_b(L,t)\, L^k dL\,, \tag{12}$$

where $V_d(L)$ is the particle deposition velocity given by equation (13) for any surface orientation and whose the limit for a vertical wall is described in equation (14).

$$V_d(L) = \frac{\mathbf{g}^+(L)\cdot\mathbf{n}\; u*}{1-\exp\left(\mathbf{g}^+(L)\cdot\mathbf{n}\; I_p(L)\right)}, \tag{13}$$

$$V_d(L) = \frac{u*}{I_p(L)}. \tag{14}$$

In equations (13) and (14), $u*$ is the fluid-wall friction velocity, $\mathbf{g}^+(L) = \mathbf{g}\tau_p(L)/u*$ is the dimensionless gravitational acceleration vector, $\mathbf{n}$ is the unitary normal vector to the wall and $I_p(L)$ is a function defined by:

$$I_p(L) = \frac{Sc_T}{\kappa}\ln\left(y^+\right) + \left(\frac{\tau_p^{+2}(L)}{1700} + \frac{Sc_B(L)^{-2/3}}{13.7}\right)^{-1}, \tag{15}$$

where κ is the Von Kàrmàn constant equal to 0.41, $\tau_p^+(L)$ is the dimensionless particle relaxation time defined by $\tau_p^+(L) = \tau_p(L)u^{*2}/\nu_f$, for which ν_f denotes the fluid kinematic viscosity. For the entire size range of interest, the particle relaxation time $\tau_p(L)$ is defined by:

$$\tau_p(L) = \frac{\rho_p L^2 Cu(L)}{18\mu_f} \tag{16}$$

In equation (15), $Sc_B(L)$ represents the Brownian Schmidt number such as $Sc_B(L) = \nu_f / D_B(L)$. In practice, the bulk concentration $n_b(L,t)$ appearing in equation (12) is chosen in the first near-wall cell. The size of this cell is specified as its center follows the constraint $y^+ > 30$, where y^+ is the dimensionless wall distance, according to the practical recommendation of Nerisson et al. (2011). The implementation of the complete model into a commercial CFD solver is further detailed in Guichard et al. (2014a). In the present paper, this model was implemented in the commercial code ANSYS Fluent 15.0.

3.4. Linking non-spherical particle diameters

3.4.1. Volume equivalent and electrical mobility diameters

The model described in this section considers volume equivalent diameters, whereas the experimental measurements of Belut and Christophe (2016) correspond to mobility diameters. Diameters must hence be translated for the sake of comparison. A commonly used relationship between the volume equivalent diameter L and the electrical mobility diameter L_m is given by DeCarlo et al. (2004) as:

$$\frac{L_m}{Cu\left(L_m\right)} = \chi \frac{L}{Cu\left(L\right)}, \tag{17}$$

where $Cu\left(L\right)$ is the Cunningham coefficient obtained from equation and χ is the dynamic shape factor. Equation (17) can be solved for each aerosol knowing the mean dynamic shape factor of aggregates. Belut and Christophe (2016) provide the ratio between the Feret's diameter and the projected area diameter resulting from a TEM analysis. Assuming that such ratio gives an estimate of the dynamic shape factor, the value of 1.08 is retained for the *NaCl* aerosol, corresponding to fairly compact aggregates, and the value of 1.90 will be used for the *CuO* aerosol. These dynamic shape factors are consistent with the literature (Hinds, 1982) and with the TEM images of Belut and Christophe (2016).

In practice, the link between volume equivalent and mobility diameters is used in the computation through the following steps:

- Pre-processing: equation (17) is used to convert a measured particle size distribution (as a function of electrical mobility diameter) to a modeled particle size distribution (as a function of volume equivalent diameter)
- Calculation: equation (5) is fully solved in terms of volume equivalent diameters, which also allows assuring a perfect mass balance.
- Post-processing: if numerical results have to be compared with measurements, it is possible to go back to electrical mobility diameters by re-using equation (17).

3.4.2. Volume equivalent and geometrical diameters

Numerical simulations require the definition of a geometrical diameter L_g which is involved in the aggregation kernel expression of equation (5). For fractal-like aggregates, L_g takes the following form:

$$L_g = L_0 N_0^{\,1/D_f}, \tag{18}$$

where L_0 is the mean monomer diameter, D_f is the fractal dimension and N_0 is the number of monomers per aggregate given by:

$$N_0 = \frac{1}{\varphi}\left(\frac{L}{L_0}\right)^3, \tag{19}$$

where φ is the packing fraction taken to 0.68, close to the densest packing limit of about 0.74. This factor takes into account the fact that spherical monomers cannot occupy the whole aggregate volume. The mean diameter of monomers can be measured from TEM images and the fractal dimension is usually deduced from simultaneous measurements of two equivalent diameters. Charvet et al. (2014) obtained a monomer diameter of 2.6±0.6 nm and a mass-mobility exponent of 2.174 for *Cu* and *CuO* aerosols produced by the spark discharge generator used in Belut and Christophe (2016). The mass-mobility exponent differs from the fractal dimension, but Eggersdorfer et al. (2012) found that an aggregate with a mass-mobility exponent of 2.15 also has a fractal dimension of 1.8. Hence a monomer diameter of 2.6 nm and a fractal dimension of 1.8 will be used in *CuO* simulations. Regarding *NaCl* nanoparticles generated by nebulization, we use the parameters of Guichard et al. (2014a) which showed a good agreement with experimental data for a monomer diameter of 10 nm and a fractal dimension of 2.2. These values are consistent with the compact shape of *NaCl* aggregates observed by Belut and Christophe (2016).

In practice, the link between volume equivalent and geometrical diameters is used while computing the aggregation source term with equation (5). Abscissas L and weights w are first obtained from moments M_k according to the quadrature method of moments. Then equation (18) is used to convert volume equivalent abscissas to geometrical abscissas where it is required in the aggregation kernel computation, namely in equations (7), (8) and (9).

4. Summary: parameters used in the simulations

Table 1 summarizes the input parameters obtained from the experiment and used to simulate the two considered cases.

Table 1 Input parameters used in CFD simulations

Material	Re_H	Inlet bulk velocity ($m.s^{-1}$)	k ($m^2.s^{-2}$)	ε ($m^2.s^{-3}$)	Particles total number concentration ($\#.cm^{-3}$)	*GMD* (nm)	*GSD* (nm)	Dynamic shape factor	Elemental density ($kg.m^{-3}$)	Monomer diameter (nm)	Fractal dimension
NaCl	15000	0.589	$4.00\ 10^{-3}$	0.0169	$6.3\ 10^{6}$	43.7	1.65	1.08	2170	10	2.2
CuO	15000	0.589	$4.00\ 10^{-3}$	0.0169	$7.13\ 10^{6}$	9.65	1.71	1.9	6315	2.6	1.8

5. Results and discussion

5.1. Validation of the modeled carrier airflow

Figure 2 shows velocity vectors superimposed with the contours of velocity magnitude on the median vertical plane of figure 1 and on a horizontal plane passing through the inlet center. A round jet is developed from the inlet and produces recirculation zones. The velocities at the center of the chamber are much lower than the velocities in the jet, which will result in spatially variable residence time and thus aggregation state of the aerosol.

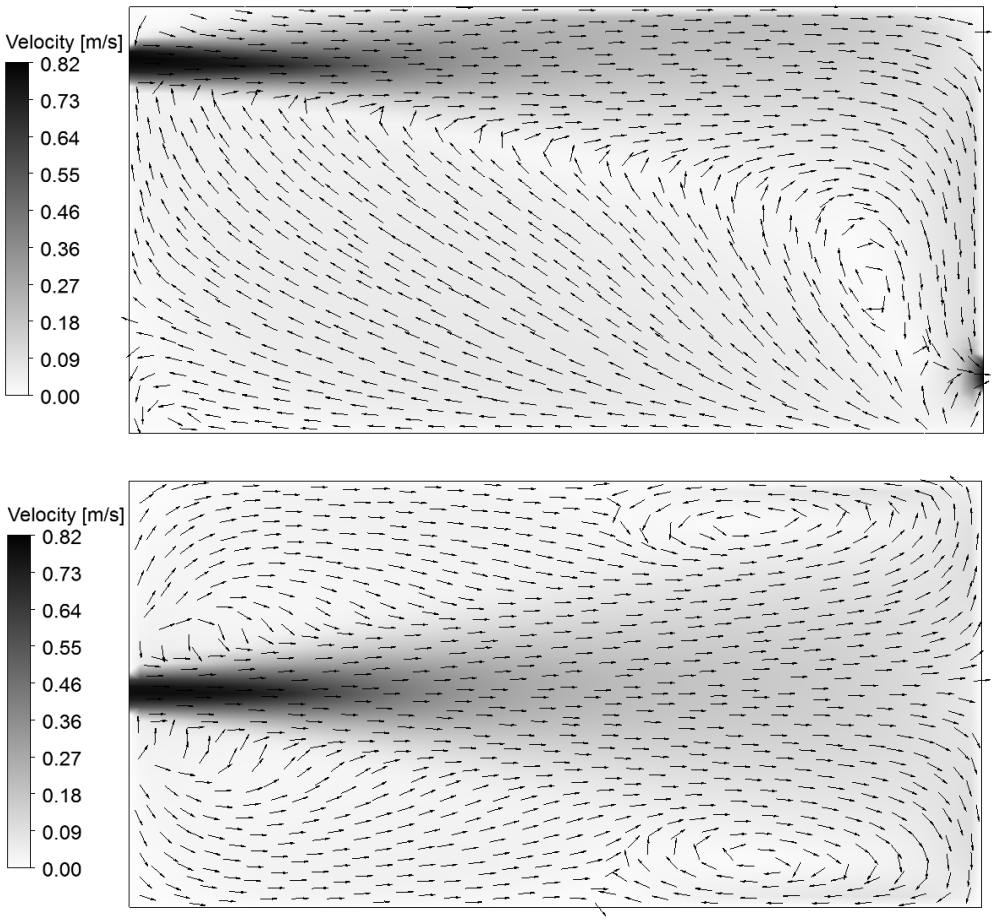

Figure 2 Overview of the airflow pattern in the chamber.
Top: Vertical plane passing through the inlet center (y=0 m).
Bottom: Horizontal plane passing through inlet center (z=0.345 m).

In order to evaluate the accuracy of the numerical simulations for the carrier gas flow, mean velocity profiles in the central plane of figure 1 are considered, at abscissas x=0.1 m, x=0.3 m, x=0.5 m and x=0.7 m. Figure 3 shows a comparison between the velocity profiles measured by LDA and computed with the RANS $k-\varepsilon$ RNG model on a coarse mesh of 70,000 cells and on a fine mesh of 500,000

cells. Both meshes leading to an accurate representation of the airflow, hence the coarse mesh of 70,000 cells will be used as a basis in following subsections.

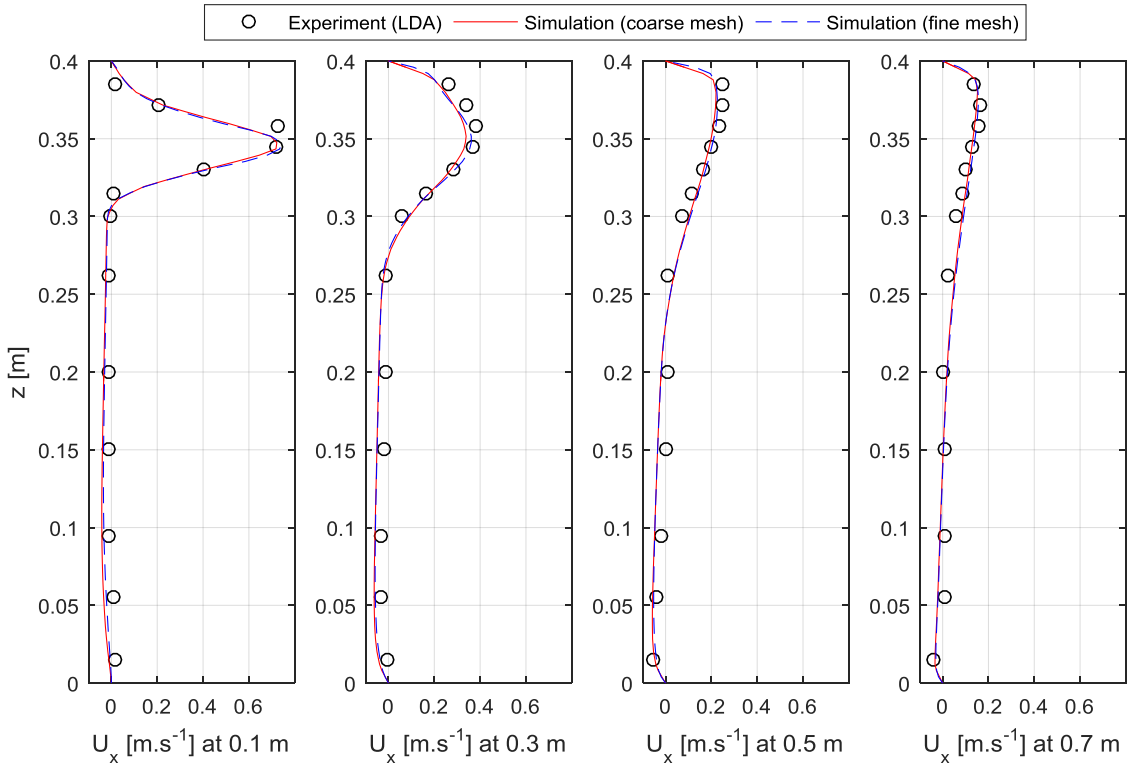

Figure 3 Measured and computed velocity profiles in the central plane (y=0 m)

LDA measurements also allow evaluating the capability of turbulence models to predict turbulence levels. Turbulence kinetic energy profiles obtained experimentally by LDA and computed by the RANS $k-\varepsilon$ RNG model are presented in figure 4. A logarithmic scale is used at abscissas since the turbulence kinetic energy changes over more than two orders of magnitude, which prevented a linear scale from highlighting discrepancies for small values of k. Results show that simulations are in quite good agreement with experimental data regarding the turbulence kinetic energy. Thus, both mean velocity and turbulence are well reproduced by current CFD simulations, which is an essential prerequisite to model aerosol transport.

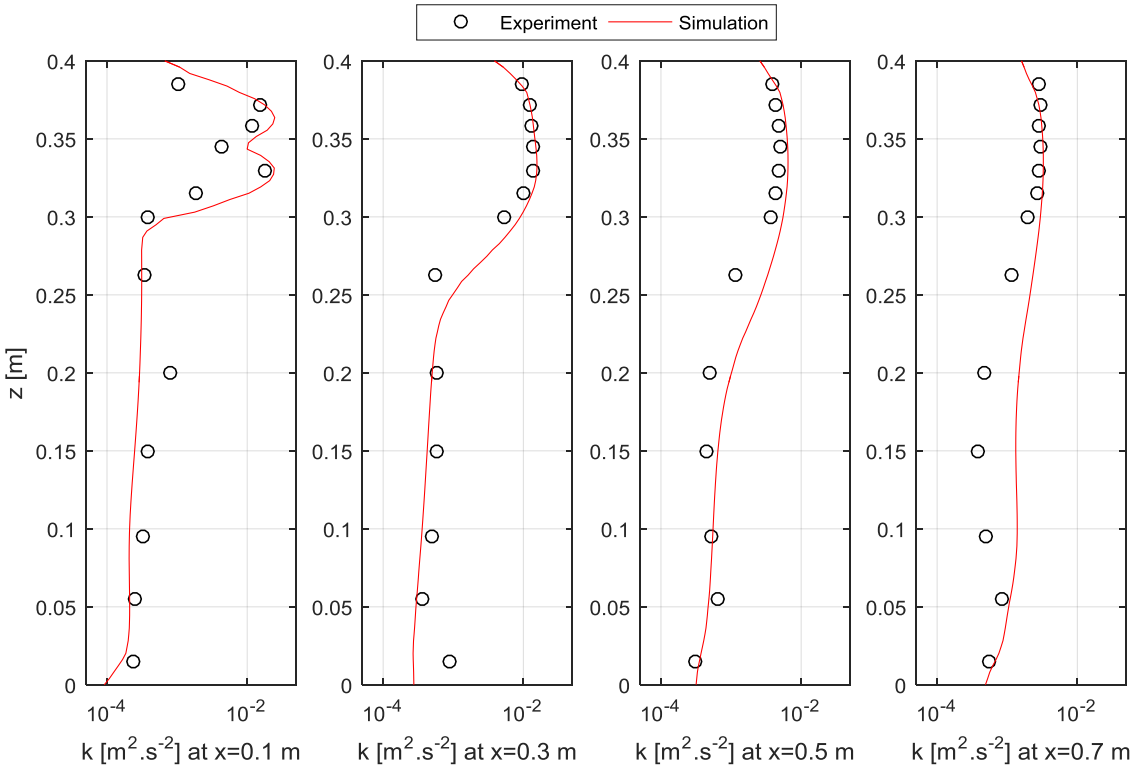

Figure 4 Measured and computed turbulence kinetic energy profiles in the central plane (y=0 m)

Measured and computed mean ages of air are also compared in figures 5 and 6 as another way to validate the simulated carrier gas flow. If the flow were perfectly mixed in the chamber, the local mean age of air would be homogenous and equal to the perfect mixing residence time τ_n where $\tau_n = V / Q$, V being the chamber volume and Q being the volume flow rate in the chamber. In the present experiment, τ_n is equal to 180 s. From the data in the middle vertical plane (y=0) in figure 5, it appears that the fresh incoming air mixes quickly in the chamber since τ_a already approaches τ_n at x=0.7 m, while presenting a low vertical heterogeneity. The computed values are in very good agreement with measurements which indicates an accurate modeling of the mean airflow and turbulence diffusivity.

Outside of the central plane, measured and computed mean ages of air are found very close to τ_n, and vary little with the horizontal position y and vertical position z, which indicates a good mixing. To illustrate compactly the comparison between measured and simulated values on these planes, figure 6 hence shows the ratio τ_a / τ_n as a function of the x abscissa, for both planes y=-0.1 m and y=0.1 m and for all considered z positions (see Belut and Christophe (2016)). Measured values are shown on figure 6a and corresponding computed values on figure 6b. The ratio τ_a / τ_n departs from unity by a maximum of about 15% for these planes. The highest ages of air are encountered for the minimum x positions but outside the jet, which is consistent with the air apparent trajectory illustrated in figure 2.

Outside the jet, as one goes in the x direction from the inlet face to the outlet face of the chamber, the mean age of air decreases to approach the perfect mixing residence time. Similar trends are found experimentally and numerically, which confirms the good representation of the modeled airflow. Considering this distribution of the mean age of air, it is expected that the aerosol PSD will strongly vary through aggregation in the jet region, while presenting rather homogenous properties in the rest of the chamber.

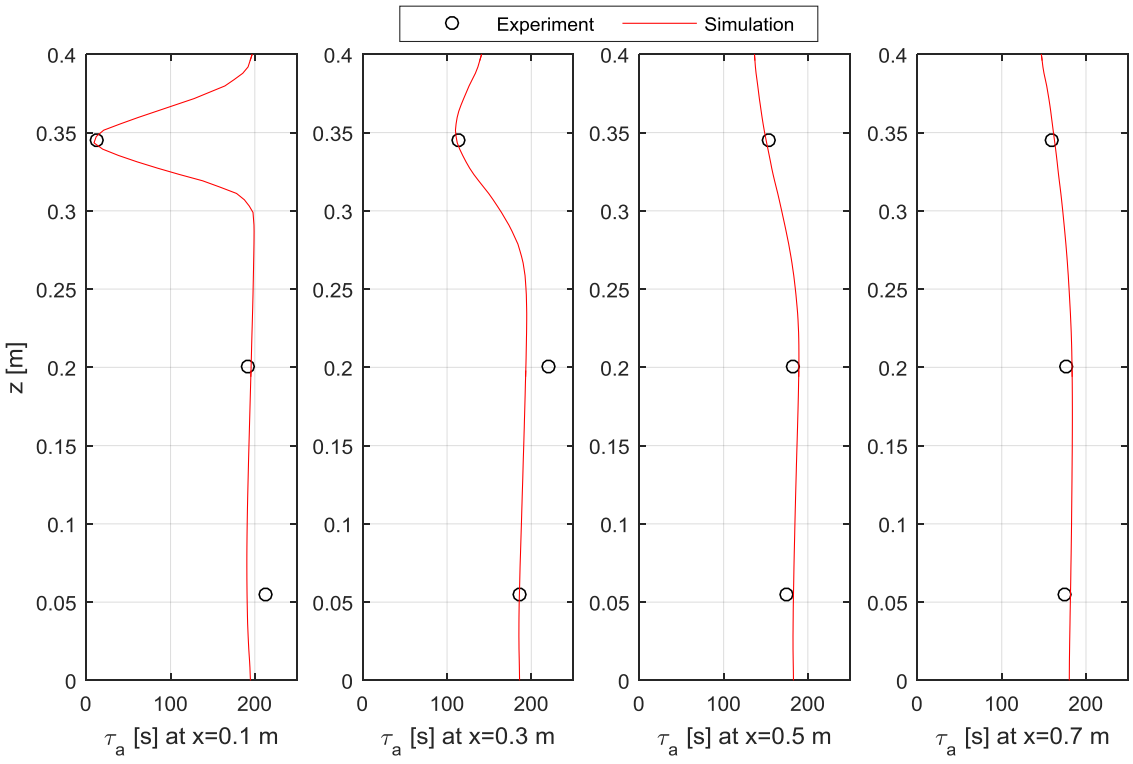

Figure 5 Measured and computed mean ages of air τ_a in the central plane (y=0 m)

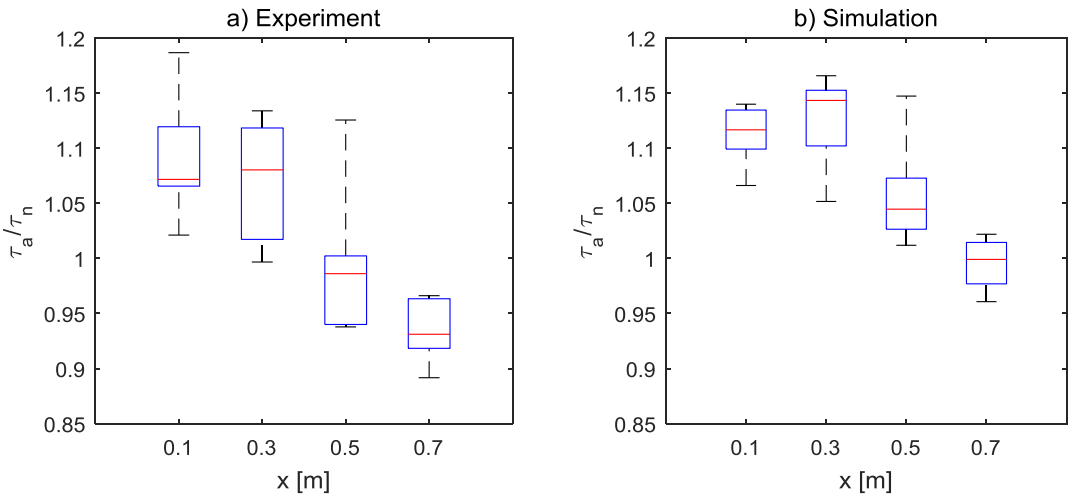

Figure 6 Ratios of τ_a / τ_n in planes y=0.1 m and y=-0.1 m: a) Experiment b) Simulation

5.2. Comparison between measured and computed particle size distributions

Figure 7 offers an overview of the nanoparticle dynamics inside the ventilated chamber by showing the contours of number concentration and geometric mean diameter (GMD) for the *NaCl* aerosol in the central plane (y=0 m). The geometric mean diameter is computed by equation (20). As expected, results highlight the decrease of the particle concentration and the increase of the mean diameter as functions of the aerosol residence time. It can thus be observed that the concentration is quite homogeneous inside the chamber, except inside the inlet jet because of the supply of fresh nanoparticles.

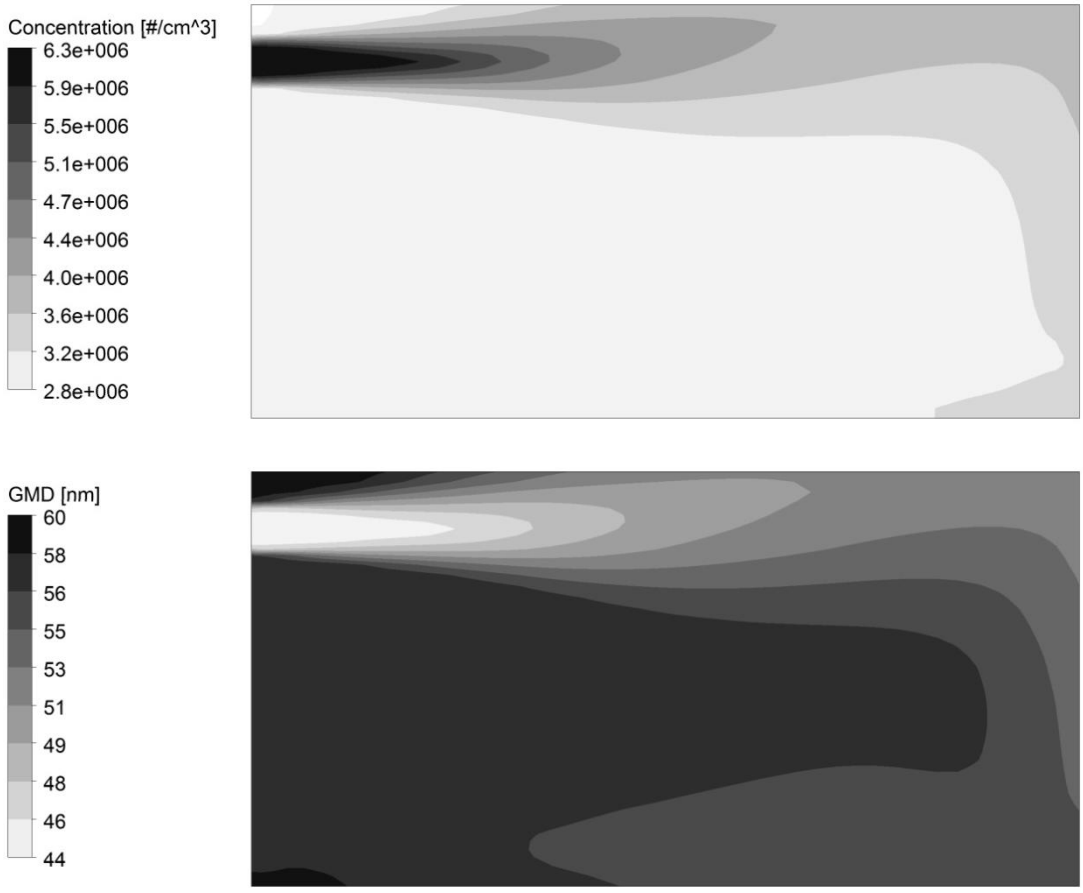

Figure 7 Contours of number concentration (Top) and geometric mean diameter (Bottom) for *NaCl* in the central plane (y=0 m)

To evaluate the relevancy of the modeling presented in section 3 for predicting the particle dynamics in a ventilated chamber, the total number concentration M_0 in the central plane at abscissas x=0.1 m, x=0.3 m, x=0.5 m and x=0.7 m is plotted in figure 8 for the *NaCl* aerosol. The number concentration between the inlet and the center of the chamber is reduced by a factor of about two, changing from 6.3×10^6 #.cm^{-3} to 3.15×10^6 #.cm^{-3}, demonstrating the impact of aggregation on airborne nanoparticles.

The numerical simulation is in very good agreement with the experimental data of Belut and Christophe (2016), where the predicted values fall within the measurement errors. However, slight discrepancies can be observed at the top of the concentration profile at x=0.7 m. Numerical results seem more sensitive to the inlet jet while experimental results are almost homogeneous along this vertical profile. Such measurements results are not totally expected because this phenomenon was not observed on mean air ages profiles in figure 5, where both numerical and experimental results were still sensitive to the inlet jet, despite approaching homogeneity. In fact, as the aerosol age is lower at z=0.35 m than at z=0.05 m, the concentration should be higher, which is not obvious on particle concentration measurements at x=0.7 m.

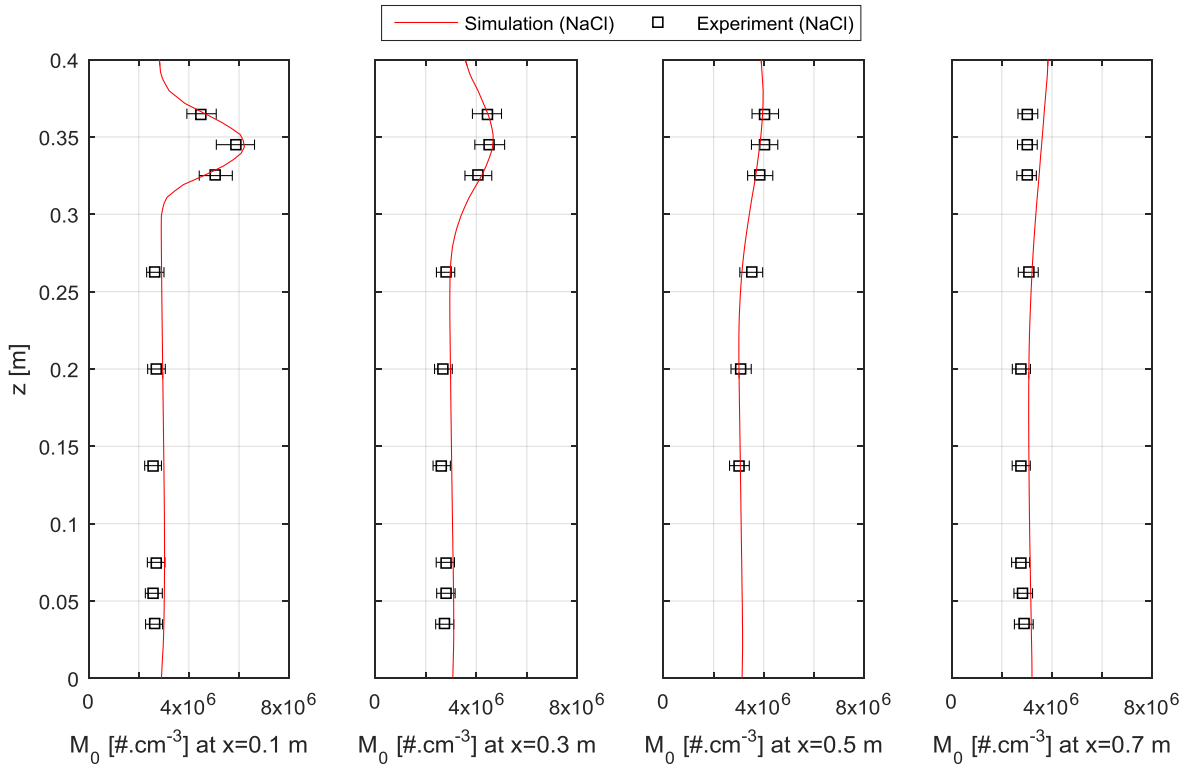

Figure 8 Measured and computed number concentrations for *NaCl* in the central plane (y=0 m)

The total number concentration M_0 in the central plane is now plotted for the *CuO* aerosol in figure 9. It can first be observed that the number concentration is divided by three between the inlet and the center of the chamber, changing from 7.13×10^6 #.cm^{-3} to about 2.30×10^6 #.cm^{-3}. This significant change in particle size distribution is explained by a higher aggregation rate than for *NaCl* particles, due to a higher number concentration at inlet, smaller particles and less compact shapes of aggregates. A high number concentration indeed increases the probability of collision between particles and a small size increases the sensitivity of particles to Brownian motion and hence particles velocity

decorrelation which lead to higher collision rates. A low effective density of aggregates also increases their sphere of influence and hence their collision likelihood.

The predicted number concentration near the inlet (at x=0.1 m) does not fit the measured number concentration for the *CuO* aerosol: measurements show an almost immediate decrease of 30% with respect to the inlet value. This finding is surprising, considering the measurements of mean ages of air in figure 5. The mean age of air at this position [x=0.1 m, y=0 m, z=0.345 m] is only of 18 s, so the number concentration should be closer to the inlet value, as observed in numerical simulations, since the aerosol did not age for a sufficient time for aggregation to become so significant. Such a quick aggregation is not consistent with the further evolution of the aerosol in the chamber. Apart from this possible experimental bias, figure 9 shows that the aerosol concentration is rather well predicted by the model throughout the chamber.

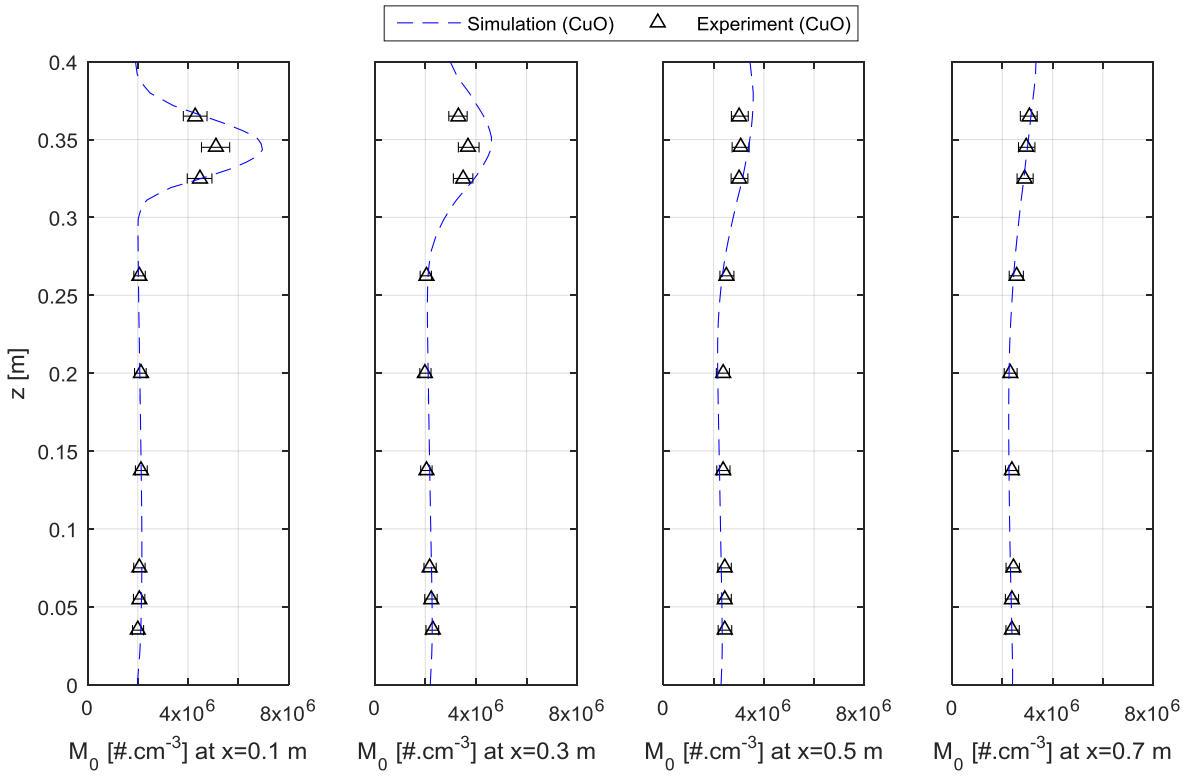

Figure 9 Measured and computed number concentrations for *CuO* in the central plane (y=0 m)

Aggregation decreases the number concentration of aerosols as a function of their residence time, as observed in figures 8 and 9. In the meantime, the mean diameter of the PSD is expected to increase while the PSD widens. Tracking the evolution of these aerosol properties between a source and its potential inhalation is an important expected feature of models designed for exposure or toxicology studies. The geometric mean diameter GMD and the geometric standard deviation GSD can be expressed as functions of moments when assuming a log-normal particle size distribution as:

$$GMD = \frac{{M_1}^2}{\sqrt{{M_0}^3 M_2}}, \tag{20}$$

$$GSD = \exp\left(\sqrt{\ln\left(\frac{M_0 M_2}{{M_1}^2}\right)}\right), \tag{21}$$

where M_0, M_1 and M_2 are the first three moments of the particle size distribution.

The log-normal assumption can be made here because correlation coefficients between fitted log-normal distributions and measured particle size distributions are above 99%.

Figure 10 presents the comparison between measured and predicted GMD for *NaCl* and *CuO* aerosols in the central plane y=0. As expected, the GMD increases as the aerosol ages in the chamber. A very good agreement is obtained between numerical and experimental results.

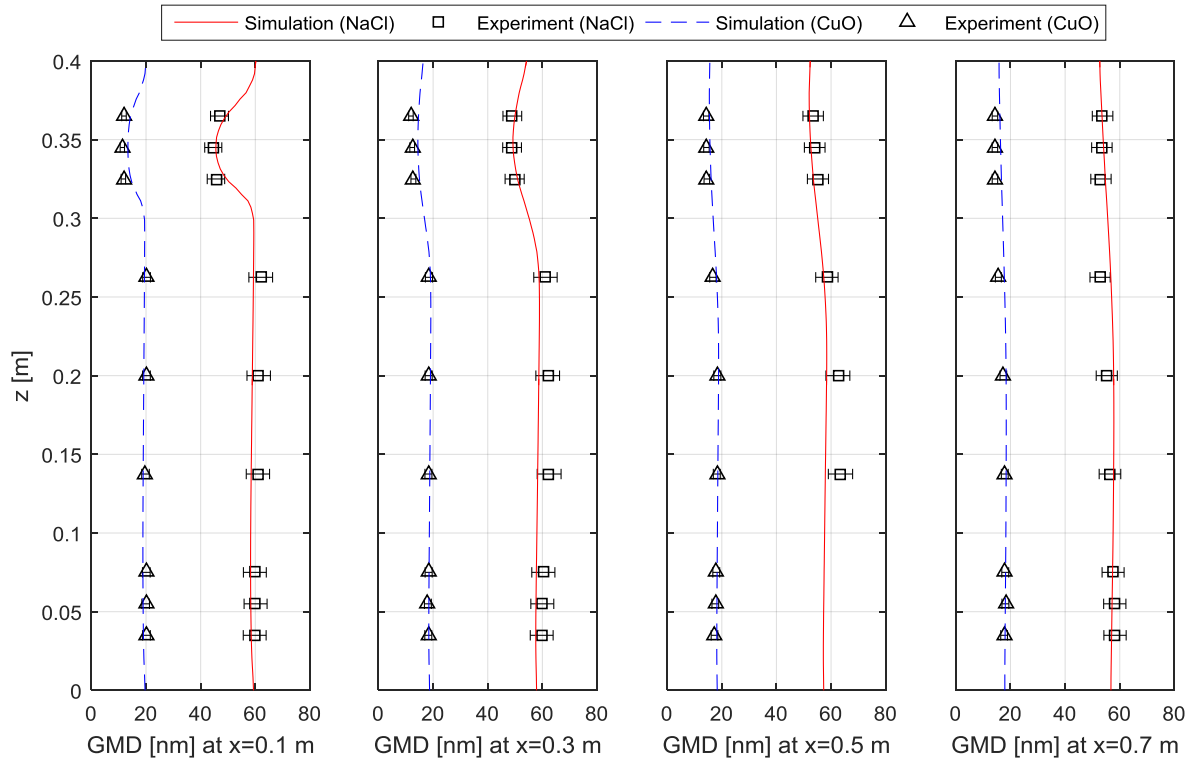

Figure 10 Measured and computed geometric mean diameters for *NaCl* and *CuO* in the central plane (y=0 m)

Figure 11 shows the comparison between measured and predicted GSD for *NaCl* and *CuO* aerosols in the central plane y=0. The aerosol PSD widens between the inlet and the outlet since the GSD increases while the particles age. It can be observed in figure 11 that numerical simulations tend to

slightly under-estimate the GSD systematically. These discrepancies are attributed to the log-normal assumption used to reconstruct particle size distributions, which is not strictly true in practice. However big the relative errors between experimental and numerical GSD appear on figure 11 because of the x-axis scale, they in fact do not exceed 5% which is a fairly acceptable modeling error.

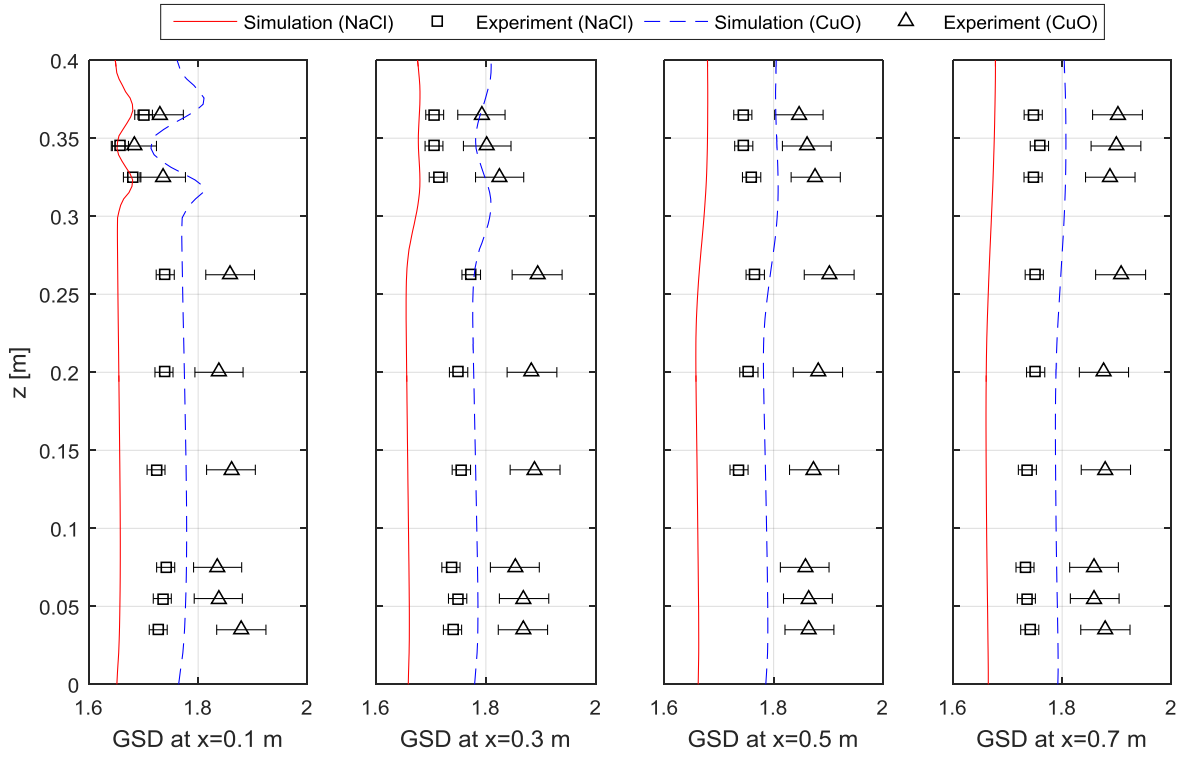

Figure 11 Measured and computed geometric standard deviations for *NaCl* and *Cu* in the central plane (y=0 m)

Beyond the mere prediction of the evolution of the aerosol global properties (total number concentration, GMD and GSD), it can also be useful to reconstruct the real particle size distribution from the moments. Presuming again a log-normal distribution according to the measurements, the number probability density function (PDF) can be explicitly computed from the moments with the following equation:

$$n(L) = \frac{1}{L\sqrt{2\pi}\ln(GSD)} \exp\left(-\frac{\ln^2(L/GMD)}{2\ln^2(GSD)}\right). \quad (22)$$

Figure 12 thus shows the measured and computed PDFs of diameters for both *NaCl* and *CuO* aerosols at inlet and outlet. At inlet, the reconstructed PDF from simulation results is expected to be similar to the measured one since it constitutes a simulation input. The small differences which can be observed are due to the presumed log-normal distribution which does not perfectly fit measurements. However,

these results demonstrate that the modeling is able to quantitatively predict the change of particle size distribution resulting from the aggregation occurring during the turbulent transport of an aerosol of ultrafine particles.

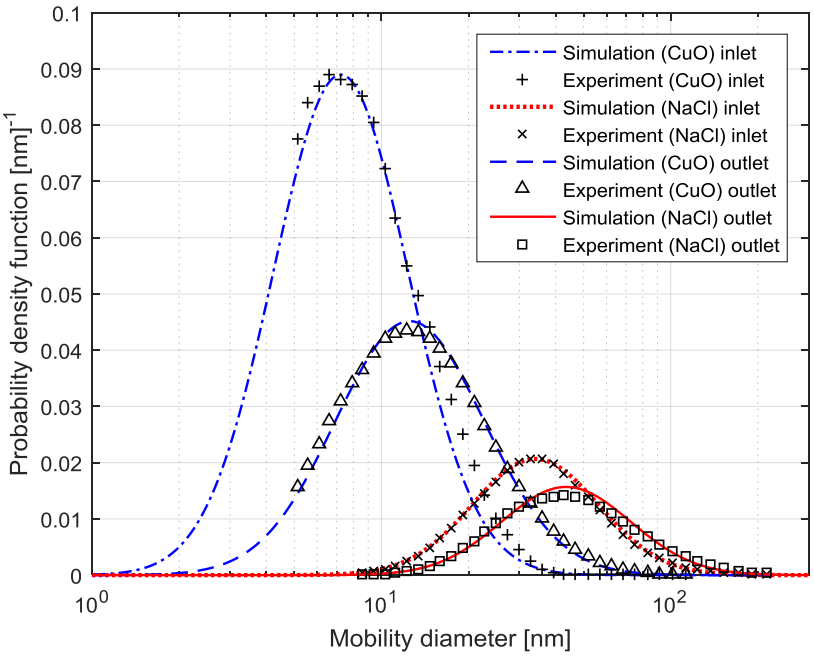

Figure 12 Measured and computed probability density functions at inlet and outlet of *NaCl* and *CuO* aerosols

5.3. Computed deposition losses

The modeling approach allows distinguishing the reduction of nanoparticles due to deposition and aggregation. It is hence possible to post-process the rate of particles which are entering the chamber, exiting the chamber, depositing on the walls and aggregating between them at each time. Such rates are summarized in table 2. From this table, it can be observed that only 0.18 % of the emitted *NaCl* nanoparticles are lost by deposition, whereas 48.13 % are lost by aggregation. For the *CuO* aerosol, it is 1.07 % by deposition and 63.82 % by aggregation. These results tend to confirm the minor contribution of particle deposition compared to particle aggregation in the chamber.

To distinguish the relative contribution of Brownian and turbulent aggregation rates, computations using a pure Brownian aggregation kernel have also been conducted. For the present application, it can be observed in table 2 that the contribution of turbulence on aggregation is negligible because of the low inertia of particles and of the globally low turbulence intensity in the chamber. The contribution of turbulence is slightly higher for the aggregation of the *NaCl* aerosol, although it stays below the deposition contribution. Thus, in present case, turbulent aggregation doesn't play a significant role.

However, it still has to be taken into account for other applications where turbulence is more intense, such as demonstrated by the experiment of Kim et al. (2006) which involved aerosol of similar PSD, shape and composition at higher turbulence intensities.

Table 2 Balance of incoming and outgoing rates of particles in the ventilated chamber

Material	Inlet rate ($\#.s^{-1}$) $\times 10^9$	Outlet rate ($\#.s^{-1}$) $\times 10^9$	Deposition rate ($\#.s^{-1}$) $\times 10^9$	Number reduction due to pure Brownian aggregation ($\#.s^{-1}$) $\times 10^9$	Number reduction attributable to turbulent aggregation ($\#.s^{-1}$) $\times 10^9$
	I	**II**	**III**	**IV**	**I-II-III-IV**
NaCl	4.538	2.346	0.008	2.182	0.002
CuO	5.136	1.803	0.055	3.277	0.001

Numerical simulations offer a powerful tool to identify locations where the deposition of nanoparticles is the most important. The distribution of the flux of *CuO* particles which are deposited to the walls is thus shown in figure 13 for planes at y=0.2 m (rear wall), z=0 m (ground) and x=0.8 m (outlet wall). Hence, for such low-inertia particles, the highest deposition rate is reached on vertical walls for the viewing planes in figure 13. This fact is expected because the deposition mainly occurs from the contribution of turbulent and Brownian mechanisms.

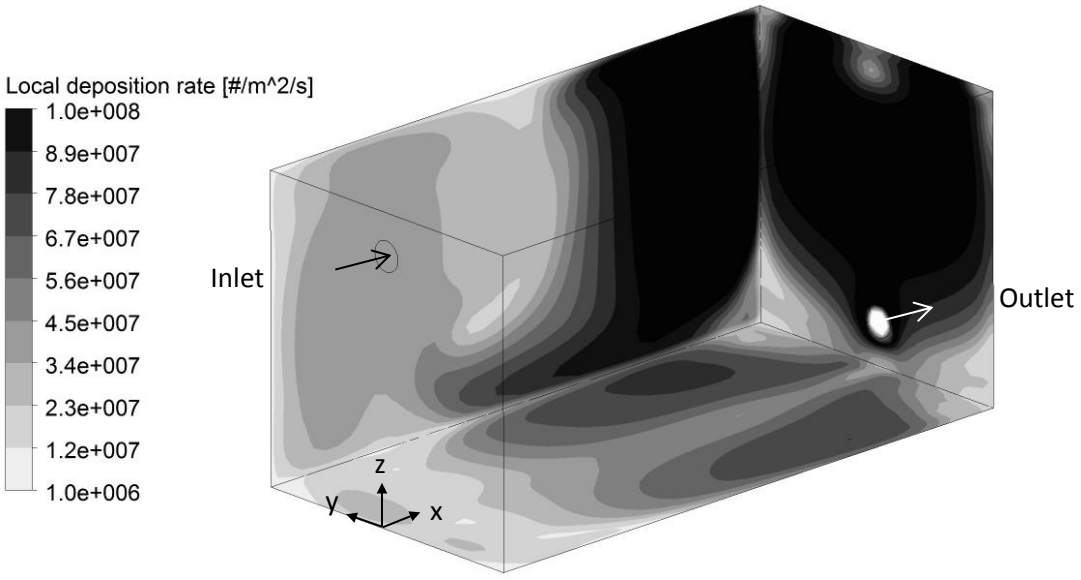

Figure 13 Computed local deposition rate for the *CuO* aerosol

6. Conclusion

The CFD-QMOM three-dimensional modeling of the turbulent transport of airborne nanoparticles undergoing aggregation has been assessed on a comprehensive experimental dataset. The experiment was designed to provide space-resolved measurements of particles and airflow properties in a ventilated chamber operating in steady-state regime.

In a first step, mean velocity, turbulence kinetic energy and mean age of air profiles, obtained from experiments and simulations have been compared to verify the modeled airflow. Then the simulation of the dynamics of two different aerosols has been validated by comparing measured and computed characteristics of the aerosols particle size distributions. The modeling approach was found to provide satisfactory predictions of the particle size distributions for all considered cases, given the experimental uncertainties.

The presented CFD-QMOM approach appears hence able to predict convincingly the behavior of an aerosol of nanoparticles subjected to turbulent transport, deposition and aggregation. Such modeling can be used to track the particle size distribution of a nano-sized aerosol from its emission to the whole indoor environment, with immediate applications in the field of exposure modeling and computer aided design of protective equipments or ventilation strategies. As this model has also been validated for micro-sized aerosols undergoing transport, deposition and sedimentation in a recent paper (Guichard et al., 2014a), the use of this modeling approach extends to various indoor situations where aerosol size ranges from a few nanometers to a few micrometers.

7. References

Allen, T., 2003. Powder Sampling and Particle Size Determination. Elsevier.

Alopaeus, V., Laakkonen, M., Aittamaa, J., 2006. Numerical solution of moment-transformed population balance equation with fixed quadrature points. Chem. Eng. Sci. 61, 4919–4929. doi:10.1016/j.ces.2006.03.028

Barrett, J.C., Jheeta, J.S., 1996. Improving the accuracy of the moments method for solving the aerosol general dynamic equation. J. Aerosol Sci. 27, 1135–1142. doi:10.1016/0021-8502(96)00059-6

Belut, E., Christophe, T., 2016. A new experimental dataset to validate CFD models of airborne nanoparticles agglomeration. Presented at the 9th International Conference on Multiphase Flow, Firenze, Italy.

Berlemont, A., Achim, P., Chang, Z., 2001. Lagrangian approaches for particle collisions: The colliding particle velocity correlation in the multiple particles tracking method and in the stochastic approach. Phys. Fluids 1994-Present 13, 2946–2956. doi:10.1063/1.1396845

Charvet, A., Bau, S., Coy, N.E.P., Bémer, D., Thomas, D., 2014. Characterizing the effective density and primary particle diameter of airborne nanoparticles produced by spark discharge using mobility and mass measurements (tandem DMA/APM). J. Nanoparticle Res. 16, 1–11.

Chen, F., Yu, S.C.M., Lai, A.C.K., 2006. Modeling particle distribution and deposition in indoor environments with a new drift–flux model. Atmos. Environ. 40, 357–367. doi:http://dx.doi.org/10.1016/j.atmosenv.2005.09.044

Cheng, J., Yang, C., Mao, Z.-S., Zhao, C., 2009. CFD Modeling of Nucleation, Growth, Aggregation, and Breakage in Continuous Precipitation of Barium Sulfate in a Stirred Tank. Ind. Eng. Chem. Res. 48, 6992–7003. doi:10.1021/ie9004282

Cheng, J.C., Fox, R.O., 2010. Kinetic Modeling of Nanoprecipitation using CFD Coupled with a Population Balance. Ind. Eng. Chem. Res. 49, 10651–10662. doi:10.1021/ie100558n

Claudotte, L., Rimbert, N., Gardin, P., Simonnet, M., Lehmann, J., Oesterlé, B., 2010. A multi-QMOM framework to describe multi-component agglomerates in liquid steel. AIChE J. 56, 2347–2355. doi:10.1002/aic.12170

DallaValle, J.M., 1952. Exhaust hoods. Industrial Press, New York.

DeCarlo, P.F., Slowik, J.G., Worsnop, D.R., Davidovits, P., Jimenez, J.L., 2004. Particle Morphology and Density Characterization by Combined Mobility and Aerodynamic Diameter Measurements. Part 1: Theory. Aerosol Sci. Technol. 38, 1185–1205. doi:10.1080/027868290903907

Eggersdorfer, M.L., Kadau, D., Herrmann, H.J., Pratsinis, S.E., 2012. Aggregate morphology evolution by sintering: Number and diameter of primary particles. J. Aerosol Sci. 46, 7–19. doi:10.1016/j.jaerosci.2011.11.005

Elghobashi, S., 1994. On Predicting Particle-Laden Turbulent Flows. Appl. Sci. Res. 52, 309.

Fox, R.O., Laurent, F., Massot, M., 2008. Numerical simulation of spray coalescence in an Eulerian framework: Direct quadrature method of moments and multi-fluid method. J. Comput. Phys. 227, 3058–3088. doi:10.1016/j.jcp.2007.10.028

Frenklach, M., 2002. Method of moments with interpolative closure. Chem. Eng. Sci., Population balance modelling of particulate systems 57, 2229–2239. doi:10.1016/S0009-2509(02)00113-6

Friedlander, S.K., others, 2000. Smoke, dust, and haze. Oxford university press New York.

Fuchs, N.A., 1964. The Mechanics of Aerosols. Pergamon Press.

Gao, N., Niu, J., 2007. Modeling particle dispersion and deposition in indoor environments. Atmos. Environ. 41, 3862–3876.

Gimbun, J., Nagy, Z.K., Rielly, C.D., 2009. Simultaneous quadrature method of moments for the solution of population balance equations, using a differential algebraic equation framework. Ind. Eng. Chem. Res. 48, 7798–7812.

Guichard, R., Belut, E., Rimbert, N., Tanière, A., 2014a. Evaluation of a Moments-based Formulation for the Transport and Deposition of Small Inertia Aerosols. J. Comput. Multiph. Flows 6, 407–418.

Guichard, R., Tanière, A., Belut, E., Rimbert, N., 2014b. Simulation of nanoparticle coagulation under Brownian motion and turbulence in a differential–algebraic framework: Developments and applications. Int. J. Multiph. Flow 64, 73–84.

Hinds, W.C., 1982. Aerosol Technology: Properties, Behavior, and Measurement of Airborne Particles. John Wiley & Sons.

Hoet, P.H., Brüske-Hohlfeld, I., Salata, O.V., 2004. Nanoparticles – known and unknown health risks. J. Nanobiotechnology 2, 1–15. doi:10.1186/1477-3155-2-12

Holmberg, S., Chen, Q., 2003. Air flow and particle control with different ventilation systems in a classroom. Indoor Air 13, 200–204.

Holmberg, S., Li, Y., 1998. Modelling of the Indoor Environment – Particle Dispersion and Deposition. Indoor Air 8, 113–122. doi:10.1111/j.1600-0668.1998.t01-2-00006.x

Hulburt, H.M., Katz, S., 1964. Some problems in particle technology: A statistical mechanical formulation. Chem. Eng. Sci. 19, 555–574.

John, V., Angelov, I., Öncül, A.A., Thévenin, D., 2007. Techniques for the reconstruction of a distribution from a finite number of its moments. Chem. Eng. Sci. 62, 2890–2904. doi:10.1016/j.ces.2007.02.041

Kim, D., Hong, S., Kim, Y., Lee, K., 2006. Deposition and coagulation of polydisperse nanoparticles by Brownian motion and turbulence. J. Aerosol Sci. 37, 1781–1787.

Kim, D., Park, S., Song, Y., Kim, D., Lee, K., 2003. Brownian coagulation of polydisperse aerosols in the transition regime. J. Aerosol Sci. 34, 859–868.

Koivisto, A.J., Yu, M., Hämeri, K., Seipenbusch, M., 2012. Size resolved particle emission rates from an evolving indoor aerosol system. J. Aerosol Sci. 47, 58–69.

Kostoglou, M., 2007. Extended cell average technique for the solution of coagulation equation. J. Colloid Interface Sci. 306, 72–81. doi:10.1016/j.jcis.2006.10.044

Kumar, J., Peglow, M., Warnecke, G., Heinrich, S., Mörl, L., 2006. Improved accuracy and convergence of discretized population balance for aggregation: The cell average technique. Chem. Eng. Sci. 61, 3327–3342. doi:10.1016/j.ces.2005.12.014

Kumar, S., Ramkrishna, D., 1996. On the solution of population balance equations by discretization—I. A fixed pivot technique. Chem. Eng. Sci. 51, 1311–1332. doi:10.1016/0009-2509(96)88489-2

Lambin, P., Gaspard, J.-P., 1982. Continued-fraction technique for tight-binding systems. A generalized-moments method. Phys. Rev. B 26, 4356.

Laurent, F., Massot, M., Villedieu, P., 2004. Eulerian multi-fluid modeling for the numerical simulation of coalescence in polydisperse dense liquid sprays. J. Comput. Phys. 194, 505–543. doi:10.1016/j.jcp.2003.08.026

Lee, K.W., Chen, J., Gieseke, J.A., 1984. Log-Normally Preserving Size Distribution for Brownian Coagulation in the Free-Molecule Regime. Aerosol Sci. Technol. 3, 53–62. doi:10.1080/02786828408958993

Marchisio, D.L., Fox, R.O., 2013. Computational models for polydisperse particulate and multiphase systems. Cambridge University Press.

Marchisio, D.L., Fox, R.O., 2005. Solution of population balance equations using the direct quadrature method of moments. J. Aerosol Sci. 36, 43–73. doi:10.1016/j.jaerosci.2004.07.009

Marchisio, D.L., Vigil, R.D., Fox, R.O., 2003b. Implementation of the quadrature method of moments in CFD codes for aggregation–breakage problems. Chem. Eng. Sci. 58, 3337–3351. doi:10.1016/S0009-2509(03)00211-2

Marchisio, D.L., Pikturna, J.T., Fox, R.O., Vigil, R.D., Barresi, A.A., 2003a. Quadrature method of moments for population-balance equations. AIChE J. 49, 1266–1276.

McGraw, R., 1997. Description of aerosol dynamics by the quadrature method of moments. Aerosol Sci. Technol. 27, 255–265.

Mohaupt, M., Minier, J.-P., Tanière, A., 2011. A new approach for the detection of particle interactions for large-inertia and colloidal particles in a turbulent flow. Int. J. Multiph. Flow 37, 746–755. doi:10.1016/j.ijmultiphaseflow.2011.02.003

Mulholland, G.W., Baum, H.R., 1980. Effect of Initial Size Distribution on Aerosol Coagulation. Phys. Rev. Lett. 45, 761–763. doi:10.1103/PhysRevLett.45.761

Nerisson, P., Simonin, O., Ricciardi, L., Douce, A., Fazileabasse, J., 2011. Improved CFD transport and boundary conditions models for low-inertia particles. Comput. Fluids 40, 79–91.

Oberdörster, G., Maynard, A., Donaldson, K., Castranova, V., Fitzpatrick, J., Ausman, K., Carter, J., Karn, B., Kreyling, W., Lai, D., Olin, S., Monteiro-Riviere, N., Warheit, D., Yang, H., 2005. Principles for characterizing the potential human health effects from exposure to nanomaterials: elements of a screening strategy. Part. Fibre Toxicol. 2, 1–35. doi:10.1186/1743-8977-2-8

Prat, O.P., Ducoste, J.J., 2006. Modeling spatial distribution of floc size in turbulent processes using the quadrature method of moment and computational fluid dynamics. Chem. Eng. Sci., Advances in population balance modellingSecond International Conference on Population Balance Modelling 61, 75–86. doi:10.1016/j.ces.2004.11.070

Pratsinis, S.E., 1988. Simultaneous nucleation, condensation, and coagulation in aerosol reactors. J. Colloid Interface Sci. 124, 416–427. doi:10.1016/0021-9797(88)90180-4

Seipenbusch, M., Binder, A., Kasper, G., 2008. Temporal evolution of nanoparticle aerosols in workplace exposure. Ann. Occup. Hyg. 52, 707–716.

Shih, T.H., Liou, W.W., Shabbir, A., Yang, Z., Zhu, J., 1995. A New k-epsilon Eddy-Viscosity Model for High Reynolds Number Turbulent Flows - Model Development and Validation. Comput. Fluids 227–238.

Smoluchowski, M., 1917. Versuch einer mathematischen Theorie der Koagulationskinetik kolloider Lösungen.

Sommerfeld, M., 2001. Validation of a stochastic Lagrangian modelling approach for inter-particle collisions in homogeneous isotropic turbulence. Int. J. Multiph. Flow 27, 1829–1858. doi:10.1016/S0301-9322(01)00035-0

Sung, Y., Raman, V., Fox, R.O., 2011. Large-eddy-simulation-based multiscale modeling of TiO2 nanoparticle synthesis in a turbulent flame reactor using detailed nucleation chemistry. Chem. Eng. Sci., Multiscale Simulation 66, 4370–4381. doi:10.1016/j.ces.2011.04.024

Wang, L., Vigil, R.D., Fox, R.O., 2005. CFD simulation of shear-induced aggregation and breakage in turbulent Taylor–Couette flow. J. Colloid Interface Sci. 285, 167–178. doi:10.1016/j.jcis.2004.10.075

Wentzel, M., Gorzawski, H., Naumann, K.-H., Saathoff, H., Weinbruch, S., 2003. Transmission electron microscopical and aerosol dynamical characterization of soot aerosols. J. Aerosol Sci. 34, 1347–1370.

Wichmann, H.-E., Peters, A., 2000. Epidemiological evidence of the effects of ultrafine particle exposure. Philos. Trans. R. Soc. Lond. Math. Phys. Eng. Sci. 358, 2751–2769. doi:10.1098/rsta.2000.0682

Williams, M.M.R., 1985. On the modified gamma distribution for representing the size spectra of coagulating aerosol particles. J. Colloid Interface Sci. 103, 516–527. doi:10.1016/0021-9797(85)90127-4

Yakhot, V., Orszag, S.A., Thangam, S., Gatski, T.B., Speziale, C.G., 1992. Development of turbulence models for shear flows by a double expansion technique. Phys. Fluids A 4, 1510–1520. doi:http://dx.doi.org/10.1063/1.858424

Yu, M., Lin, J., 2009. Taylor-expansion moment method for agglomerate coagulation due to Brownian motion in the entire size regime. J. Aerosol Sci. 40, 549–562.

Yu, M., Lin, J., Chan, T., 2008. A New Moment Method for Solving the Coagulation Equation for Particles in Brownian Motion. Aerosol Sci. Technol. 42, 705–713. doi:10.1080/02786820802232972

Zaichik, L.I., Solov'ev, A., 2002. Collision and coagulation nuclei under conditions of Brownian and turbulent motion of aerosol particles. High Temp. 40, 422–427.

Zhao, B., Li, X., Zhang, Z., 2004. Numerical study of particle deposition in two differently ventilated rooms. Indoor Built Environ. 13, 443–451.